Numerical simulation of bundling of helical elastic rods in a viscous fluid

Weicheng Huang [a,b,c], M. Khalid Jawed [c,*]

[a] *School of Mechanical Engineering, Southeast University, Nanjing, 211189, China*
[b] *Jiangsu Engineering Research Center of Aerospace Machinery, Southeast University, Nanjing, 211189, China*
[c] *Department of Mechanical and Aerospace Engineering, University of California, Los Angeles, Los Angeles, California 90095, United States*

A R T I C L E   I N F O

A B S T R A C T

We introduce a numerical framework to study the fluid-structure interaction between two helical filaments rotating under low Reynolds number condition, motivated by the propulsion of bacteria using helical flagella. Our numerical framework couples the elasticity of the thin filaments, nonlocal hydrodynamic loading, and the contact between multiple elastic rods. Each of these three ingredients is respectively modeled by the Discrete Elastic Rods method (for a geometrically nonlinear description of soft filaments), Regularized Stokeslet Segments method (for the nonlocal drag force in a viscous fluid), and non-penetration condition between rod segments. Two helical rods rotating side by side attract each other and become closer because of their hydrodynamic interplay in a viscous environment. Depending on the initial distance between the two and their rotational frequency, the two filaments can come in physical contact. Exploiting the efficiency and robustness of the simulator, we perform a systematic parameter sweep to quantify the bundling behavior. The findings may shed light on the physics of the bio-locomotion of microorganisms and inspire the design of novel biomimetic soft robots.

1. Introduction

Bacteria often rely on the deformation of filamentary helical structures, called flagella, for locomotion [1,2]. The propulsion arises from a complex fluid-structure interaction between the structural flexibility of the flagellum and the viscous forces generated by the flow. This fluid-structure interaction may lead to geometrically nonlinear deformations [3–5], which in turn can be exploited for functionality, e.g. turning [6], tumbling [7], and polymorphic transformations [8,9]. One of the particular biophysical importance is a phenomenon called bundling [10–20] that may appear during the swimming of microbes consisting of multiple flagella, e.g. *Escherichia coli* and *Salmonella typhimurium* [21]. Each flagellum consists of a rotary motor embedded in the cell wall, a short flexible hook that acts as a universal joint, and a helical filament. The trajectory of an individual swimming cell consists of runs interrupted by tumbles. Since the radius of the flagellar filament is well below optical wavelengths and the motor rotation is relatively rapid, it is difficult to study the mechanics of the bundling process through systematic experiments [21]. Predictive simulation of bundling is equally challenging due to the need to incorporate the

long-range hydrodynamic interaction among multiple flagella, geometrically nonlinear deformation in the elastic rods – our model for flagella, and possible contact when two flagella come in close proximity. To mitigate the experimental challenges, scaled-up analog model experiments provide a promising path [21]. This paper focuses on overcoming the computational hurdles to achieve fast and robust simulation of this system.

Since 2000s, there has been a large number of investigations on flagellar propulsion – particularly from a single flagellum – through experiments [6,22–24], computation [3,25,26], and theory [27–30]. Recent efforts have modeled this fluid-structure interaction problem as a combination of Kirchhoff elastic rod theory [31] for the deformation of structure and Resistive Force Theory (RFT) [32,33] for the description of viscous fluid. This framework established that the flagellum can undergo a buckling instability when the rotational frequency of the flagellum exceeds a threshold value [3]. However, subsequent experiments have shown that whereas RFT provides a satisfactory qualitative description of the phenomena, an accurate quantitative analysis requires a nonlocal hydrodynamic force model that accounts for the interaction between the flow induced by distant parts of the filament to match the no-slip boundary condition on the flagellum surface [33–37]. More recently, the buckling instability of a helical elastic rod rotating in a viscous fluid was investigated [38] by a combination

* Corresponding author.
  E-mail address: khalidjm@seas.ucla.edu (M. Khalid Jawed).

of Lighthill's slender body theory (LSBT) [33] – a long-range hydrodynamic force model – and Discrete Elastic Rods (DER) method – a fast algorithm developed by the computer graphics community for the simulation of visually dramatic dynamics of hair, fur, and other rod-like structures in the animation industry [39–41]. The simulation results were quantitatively compared against experiments using scaled-up model flagella [38]. This combination of DER and LSBT was used to study the propulsion and instability in a rotating helical rod subjected to an axial flow [42] as well as the effect of a nearby rigid boundary on flagellar propulsion [43]. This framework was further improved to simulate the trajectory of uni-flagellar bacteria and bio-inspired soft robots; this study postulated the critical role of flagellar buckling in changing the swimming direction [44,45]. Besides the drag-based resistive force theory [32,33,46,47] and regularized singularity method [25,48–51], immersed boundary method [52–57] is widely used to model bacterial flagella interacting with a viscous fluid.

In comparison with simulation of uni-flagellar systems, multiple interacting flagella and their bundling clearly present a more difficult set of challenges [14]. Previous experimental investigations built macroscopic model systems consisting of flexible rotating helices in a viscous fluid to mimic the dimensionless parameters of the natural bio-locomotion system, e.g. the ratio between elastic force and viscous drag, normalized helical pitch and radius, and the Reynolds number [21,58]. In the soft robotics community, researchers considered biomimetic soft robots with multi-flagellar structure for its propulsive efficiency and directional control [59]. Despite the critical role of bundling in the propulsion of several economically important bacteria – as evidenced by the aforementioned experimental works, a predictive numerical model for systematical investigation of flagellar bundling is a challenging work [19,20,60], simply because of the difficulty in describing the geometrically nonlinear dynamics of multiple rods coupled with the hydrodynamic interaction and the non-penetration contact between two approaching rod segments.

Here, we introduce a numerical framework to study the dynamics of two helical elastic rods rotating side-by-side at a constant angular velocity in low Reynolds environment, a system similar to the one explored experimentally by [21], to analogize the flagellar propulsion in microorganisms [34]. Our numerical framework combines (i) DER algorithm for the description of elastic filaments [39,40], (ii) Regularized Stokeslet Segments (RSS) method for long-range hydrodynamic force model [51], and (iii) a penalty force-based contact model [61]. While prior works coupled LSBT with DER, we choose to replace LSBT with RSS – nodel method published in 2018 – as the hydrodynamic model; the reason is twofold: (i) numerical issues appear when simulating the interaction among multiple rods using LSBT, because of the discontinuity between the local and nonlocal hydrodynamic terms in the LSBT formulation [33]. RSS, on the other hand, formulates a continuous flow field generated by a line segment with a regularization parameter and no numerical issues appear when two rod segments become closer and contact with one another. (ii) The spatial discretization in LSBT-DER framework [38] is dictated by the ratio between the arclength of the flagellum, L, and the cross-sectional radius, r_0. The distance between two adjacent nodes – the discretization length – on the rod is required to be approximately equal to $1.65r_0$. RSS, however, allows us to choose a coarser discretization without any specific requirement on discretization length. This results in more than an order of magnitude speed-up in the computation time for the model system studied in this paper. Inclusion of physically-based contact model in the numerical framework is a novel feature of this study. To achieve non-penetration condition between two rod segments (a rod is divided into a number of segments in DER), we first perform a continuous collision detection during each time step of the simulation and iteratively include a penalty force in the equations of motion to guarantee no intersection between every pair of rod segments [61]. Similar contact formulations have been successfully applied in the computer graphics literature for geometric constraint maintenance [62], hair dynamics [63], and deformable body collision response [64]. The reliability of this simulation tool for making quantitative predictions is examined by a comparison between the previous experimentally validated LSBT-based method and the current RSS-based method. We then employ this computational method to quantify the deformation in two rotating flagella leading to bundling. Fig. 1 presents snapshots from our numerical simulation of a model setup for flagellar bundling. Through systematic parameter-space exploration, we analyze the onset of *bundling* between two soft filaments as a function of the angular velocity and the initial distance between the two flagella. We next measure the propulsive efficiency in a flagellum due to a nearby rotating flagellum. This is followed up by a sweep of geometric parameter space in biologically relevant regimes to quantify the dependence of bundling on the flagellar geometry. These observations can lead to better understanding of the presence of bundling and the resulting benefits to propulsion in microorganisms.

Our paper is organized as follows. In Section 2, we present the basis of the numerical framework. Next, we explore the buckling instability of a single helical rod rotating in a viscous fluid in Section 3 for the comparison between two hydrodynamic force models: LSBT and RSS. Then in Section 4, we systematically quantify the flagellar bundling behavior between two rotating soft filaments, with a focus on biologically relevant regimes. Finally, we present our conclusions and suggest potential avenues for future research in Section 5.

2. Numerical model

The numerical framework combines three components: (i) Discrete Elastic Rods (DER) method for the description of geometrically nonlinear deformation of soft filaments [39–41]; (ii) Regularized Stokeslet Segments (RSS) method for the nonlocal hydrodynamic force generated by slender structures in a viscous fluid [51], and (iii) a contact model for the achievement of non-penetration condition between two rod segments [61]. This section is organized as follows. A description of DER is provided in Section 2.1, and its coupling with RSS is in Section 2.2. Then in Section 2.3, we detail the procedure to include the contact model between two rod segments. Finally we discuss the overall time marching scheme of the simulation in Section 2.4.

2.1. Discrete elastic rods method

We use the DER method [39–41] to model the nonlinear dynamics of thin rods. The rod centerline is discretized into N nodes: $\mathbf{x}_0, \ldots, \mathbf{x}_{N-1}$, that correspond to $N-1$ edge vectors: $\mathbf{e}^0, \ldots, \mathbf{e}^{N-2}$, such that $\mathbf{e}^i = \mathbf{x}_{i+1} - \mathbf{x}_i$ and $i = 0, \ldots, N-2$. In DER method, we use subscripts to denote quantities associated with nodes, e.g. $\mathbf{x}_i$, and superscripts when associated with edges, e.g. $\mathbf{e}^i$. Each edge, $\mathbf{e}^i$, has an orthonormal reference frame $\{\mathbf{d}_1^i, \mathbf{d}_2^i, \mathbf{t}^i\}$ and a material frame $\{\mathbf{m}_1^i, \mathbf{m}_2^i, \mathbf{t}^i\}$; both of them share the tangent $\mathbf{t}^i = \mathbf{e}^i/|\mathbf{e}^i|$ as one of the directors. Referring to Fig. 2, the reference frame is updated at each time step through parallel transport in time, and the material frame can be obtained from a scalar twist angle θ^i. Nodal positions and twist angles constitute the $4N-1$ sized degrees of freedom (DOF) vector, $\mathbf{q} = [\mathbf{x}_0, \theta^0, \mathbf{x}_1, \ldots, \mathbf{x}_{N-2}, \theta^{N-2}, \mathbf{x}_{N-1}]^T$, of the discrete rod, where the superscript T denotes transposition. Based on this kinematic representation, in the remainder of this section, we formulate the elastic strains, elastic energies, and elastic forces.

The strains of a deformed Kirchhoff's rod are comprised of three parts: stretching, bending, and twisting. Stretching strain associ-
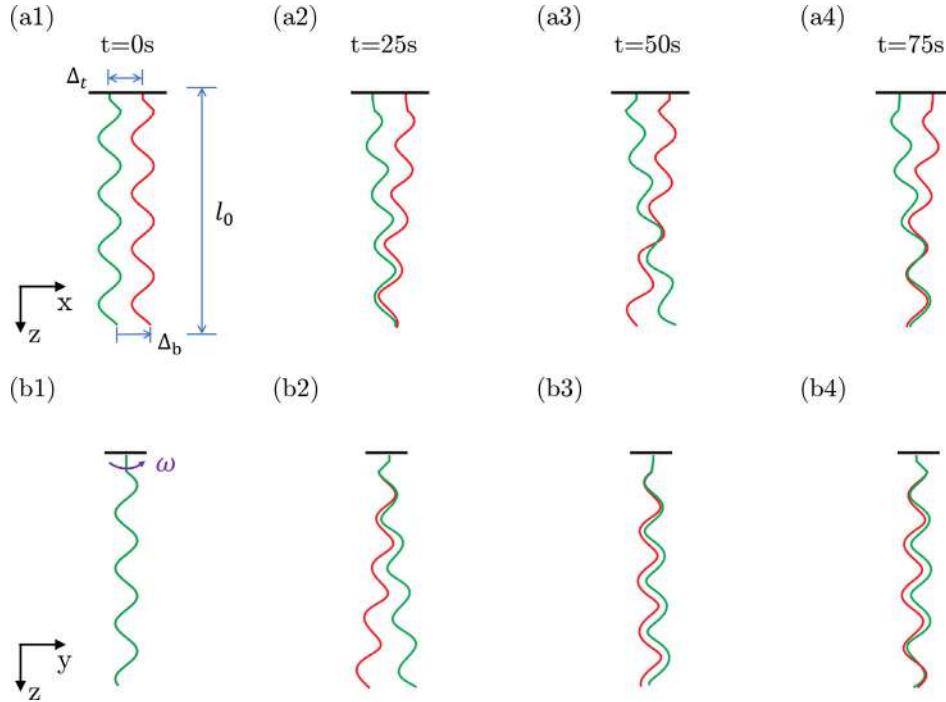
Fig. 1. Snapshots of flagellar bundling sequence. Two identical flagella rotate side by side at an angular velocity of $\omega = 15$rpm ($\bar{\omega} = 320$) with initial distance $\Delta_t = 3$cm. Physical parameters of the flagella and the fluid are provided in Section 3. (Upper) Front view and (Lower) side view of helical rods at $t \in \{0, 25, 50, 75\}$s ($\bar{t} \in \{0, 0.125, 0.250, 0.375\}$). A video showing the bundling process is provided in Supplementary Material.
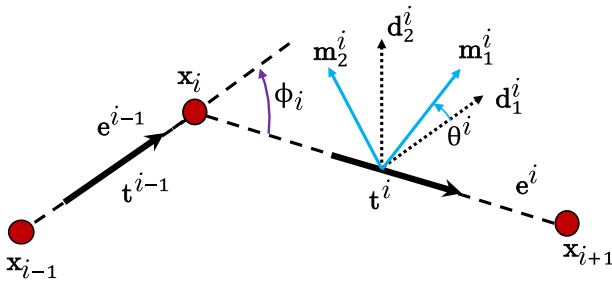
Fig. 2. Schematic of a discrete rod.

ated with the ith edge, $\mathbf{e}^i$, is

$$\epsilon^i = \frac{|\mathbf{e}^i|}{|\bar{\mathbf{e}}^i|} - 1. \tag{1}$$

Hereafter, quantities with an overbar indicate evaluation in the undeformed state, e.g. $|\bar{\mathbf{e}}^i|$ is the undeformed length of the ith edge. Bending strain is captured by the curvature binormal which measures the misalignment between two consecutive edges at a node $\mathbf{x}_i$,

$$(\kappa \mathbf{b})_i = \frac{2\mathbf{e}^{i-1} \times \mathbf{e}^i}{|\mathbf{e}^{i-1}||\mathbf{e}^i| + \mathbf{e}^{i-1} \cdot \mathbf{e}^i}, \tag{2}$$

and its norm is $|(\kappa \mathbf{b})_i| = 2 \tan (\phi_i/2)$. The material curvatures are given by the inner products between the curvature binormal and material frame vectors,

$$\kappa_i^{(1)} = \frac{1}{2}\left(\mathbf{m}_2^{i-1} + \mathbf{m}_2^i\right) \cdot (\kappa \mathbf{b})_i, \tag{3a}$$

$$\kappa_i^{(2)} = -\frac{1}{2}\left(\mathbf{m}_1^{i-1} + \mathbf{m}_1^i\right) \cdot (\kappa \mathbf{b})_i. \tag{3b}$$

The twisting strain at the ith node, in the discrete setting of DER, is measured using the discrete twist

$$\tau_i = \theta^i - \theta^{i-1} + m_i^{\mathrm{ref}}, \tag{4}$$

where m_i^{ref} is the reference twist associated with the reference frame [39].

We treat an elastic rod as a mass-spring system, with a lumped mass (and angular mass) at each node (and edge) and associated discrete stretching, bending, and twisting energies. For a rod with Young's modulus E, shear modulus G, and isotropic circular cross section, the elastic energies – stretching, bending, and twisting – are given by Bergou et al. [39,40]

$$E_s = \frac{1}{2} \sum_{i=0}^{N-2} EA(\epsilon^i)^2 |\bar{\mathbf{e}}^i| \tag{5a}$$

$$E_b = \frac{1}{2} \sum_{i=0}^{N-1} \frac{EI}{\Delta l_i}\left[(\kappa_i^{(1)} - \bar{\kappa}_i^{(1)})^2 + (\kappa_i^{(2)} - \bar{\kappa}_i^{(2)})^2\right] \tag{5b}$$

$$E_t = \frac{1}{2} \sum_{i=0}^{N-1} \frac{GJ}{\Delta l_i}(\tau_i)^2, \tag{5c}$$

where A is the area of cross-section, I is the area moment of inertia, J is the polar moment of inertia, $\Delta l_i = \left(|\bar{\mathbf{e}}^i| + |\bar{\mathbf{e}}^{i+1}|\right)/2$ is its Voronoi length.

At each degree of freedom q_j, the internal elastic forces (associated with nodal positions) and elastic moments (associated with the twist angles) are formulated by

$$F_j^{\mathrm{int}} = -\frac{\partial}{\partial q_j}(E_s + E_b + E_t), \tag{6}$$

where j is an integer between 0 to $4N - 2$. This elastic force will be balanced with external force (described in Section 2.2 and Section 2.3) and inertia to formulate the equations of motion in Section 2.4.
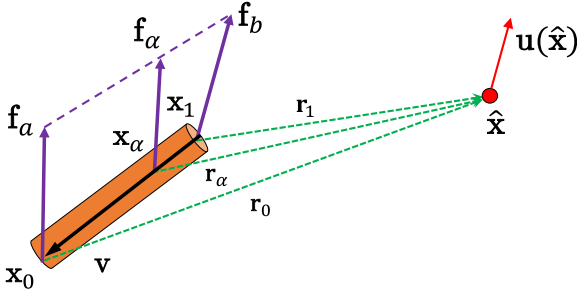
Fig. 3. Notations associated with the flow $\mathbf{u}(\hat{\mathbf{x}})$ at point $\hat{\mathbf{x}}$ generated by a line segment from $\mathbf{x}_0$ to $\mathbf{x}_1$. Note $\mathbf{r}_\alpha = \hat{\mathbf{x}} - \mathbf{x}_\alpha$ and $\mathbf{v} = \mathbf{x}_0 - \mathbf{x}_1$.

2.2. Regularized stokeslet segments method

We use RSS to model the viscous drag force experienced by a slender rod in motion within a viscous fluid. In this section, we present the relation between the velocity at each node and the hydrodynamic force applied on each node [51].

The primary Green's function (or fundamental singular solution) of Stokes flow is the Stokeslet, which describes the flow associated with a singular point force [65]. For a particular choice of regularization [48], the velocity $\mathbf{u}(\hat{\mathbf{x}})$ at evaluation point $\hat{\mathbf{x}}$ due to a regularized force $\mathbf{f}(\mathbf{x})$ applied at $\mathbf{x}$ is the regularized Stokeslet

$$8\pi\mu\mathbf{u}(\hat{\mathbf{x}}) = (\frac{1}{R} + \frac{\epsilon^2}{R^3})\mathbf{f}(\mathbf{x}) + \frac{(\mathbf{f}(\mathbf{x}) \cdot \mathbf{r})\mathbf{r}}{R^3}, \tag{7}$$

where μ is the fluid viscosity, $\mathbf{r} = \hat{\mathbf{x}} - \mathbf{x}$, $R^2 = |\mathbf{r}|^2 + \epsilon^2$, and ϵ is the regularized parameter.

Next, consider an edge of length Δl connecting the nodes $\mathbf{x}_0$ and $\mathbf{x}_1$: a point on this edge is located at $\mathbf{x}_\alpha = \mathbf{x}_0 - \alpha\mathbf{v}$ (with $\mathbf{v} = \mathbf{x}_0 - \mathbf{x}_1$ and $|\mathbf{v}| = \Delta l$). As shown in Fig. 3, we assume a linear force density $\mathbf{f}_\alpha = \mathbf{f}_a + \alpha(\mathbf{f}_b - \mathbf{f}_a)$ along the cylinder segment, such that the velocity at point $\hat{\mathbf{x}}$ due to this linear force density is,

$$8\pi\mu\mathbf{u}(\hat{\mathbf{x}}) = \Delta l \int_0^1 \left[(\frac{1}{R_\alpha} + \frac{\epsilon^2}{R_\alpha^3})\mathbf{f}_\alpha + \frac{(\mathbf{f}_\alpha \cdot \mathbf{r}_\alpha)\mathbf{r}_\alpha}{R_\alpha^3} \right]d\alpha, \tag{8}$$

where $\mathbf{r}_\alpha = \hat{\mathbf{x}} - \mathbf{x}_\alpha$ and $R_\alpha^2 = |\mathbf{r}_\alpha|^2 + \epsilon^2$. With the assumption that $\mathbf{f}_\alpha$ is a polynomial in α, the velocity in Eq. (8) can be written as [51]

$$(8\pi\mu/\Delta l)\mathbf{u}(\hat{\mathbf{x}}) = \mathbf{f}_a(T_{0,-1} + \epsilon^2 T_{0,-3}) + \mathbf{f}_b(T_{1,-1} + \epsilon^2 T_{1,-3})$$
$$+ \sum_{n=0}^{3} \mathbf{f}_n T_{n,-3}, \tag{9}$$

where the coefficients $\mathbf{f}_n$ are

$$\mathbf{f}_0 = (\mathbf{f}_a \cdot \mathbf{r}_0)\mathbf{r}_0, \tag{10a}$$

$$\mathbf{f}_1 = (\mathbf{f}_a \cdot \mathbf{v})\mathbf{r}_0 + (\mathbf{f}_a \cdot \mathbf{r}_0)\mathbf{v} + (\mathbf{f}_b \cdot \mathbf{r}_0)\mathbf{r}_0, \tag{10b}$$

$$\mathbf{f}_2 = (\mathbf{f}_a \cdot \mathbf{v})\mathbf{v} + (\mathbf{f}_b \cdot \mathbf{r}_0)\mathbf{v} + (\mathbf{f}_b \cdot \mathbf{v})\mathbf{r}_0, \tag{10c}$$

$$\mathbf{f}_3 = (\mathbf{f}_b \cdot \mathbf{v})\mathbf{v}. \tag{10d}$$

Then, the sequence of $T_{k,l}$ terms in Stokeslet Segments can be computed by the direct integration of α [51],

$$T_{0,-1} = \frac{1}{\Delta l} \log\left[\Delta l R_\alpha + (\mathbf{r}_\alpha \cdot \mathbf{v})\right]\Big|_0^1 \tag{11a}$$

$$T_{0,-3} = -\frac{1}{R_\alpha[\Delta l R_\alpha + (\mathbf{r}_\alpha \cdot \mathbf{v})]}\Big|_0^1 \tag{11b}$$

$$T_{1,-1} = \frac{R_\alpha}{(\Delta l)^2}\Big|_0^1 - \frac{(\mathbf{r}_0 \cdot \mathbf{v})}{(\Delta l)^2}T_{0,-1} \tag{11c}$$

$$T_{1,-3} = -\frac{1}{R_\alpha(\Delta l)^2}\Big|_0^1 - \frac{(\mathbf{r}_0 \cdot \mathbf{v})}{(\Delta l)^2}T_{0,-3} \tag{11d}$$

$$T_{2,-3} = -\frac{\alpha}{R_\alpha(\Delta l)^2}\Big|_0^1 + \frac{1}{(\Delta l)^2}T_{0,-1} - \frac{(\mathbf{r}_0 \cdot \mathbf{v})}{(\Delta l)^2}T_{1,-3} \tag{11e}$$

$$T_{3,-3} = -\frac{\alpha^2}{R_\alpha(\Delta l)^2}\Big|_0^1 + \frac{2}{(\Delta l)^2}T_{1,-1} - \frac{(\mathbf{r}_0 \cdot \mathbf{v})}{(\Delta l)^2}T_{2,-3} \tag{11f}$$

For completeness, we first describe the case of a continuous rod with arclength L (instead of a discrete rod composed of straight edges): consider a velocity at point $\hat{\mathbf{x}}$ due to the force field along a curve with arclength parameter, s:

$$8\pi\mu\mathbf{u}(\hat{\mathbf{x}}) = \int_0^L \left[(\frac{1}{R} + \frac{\epsilon^2}{R^3})\mathbf{f} + \frac{(\mathbf{f} \cdot \mathbf{r})\mathbf{r}}{R^3}\right]ds. \tag{12}$$

Moving on to the case of a discrete rod with N nodes and $N-1$ segments, we denote the length of ith segment as $|\mathbf{e}^i| \equiv |\mathbf{v}_i| = |\mathbf{x}_i - \mathbf{x}_{i+1}|$, and its force density (unit: force/length) as $\mathbf{f}_i$. Then the discretized version of Eq. (12) is

$$8\pi\mu\mathbf{u}(\hat{\mathbf{x}}) = \sum_{i=0}^{N-2} \left(\mathbb{A}_1^i\mathbf{f}_i + \mathbb{A}_2^i\mathbf{f}_{i+1}\right), \tag{13}$$

where $\mathbb{A}_1^i$ and $\mathbb{A}_2^i$ are 3×3 matrices:

$$\mathbb{A}_2^i = |\mathbf{v}_i|\left[(T_{1,-1}^{i,i+1} + \epsilon^2 T_{1,-3}^{i,i+1}) + T_{1,-3}^{i,i+1}(\mathbf{r}_i\mathbf{r}_i^T) + T_{2,-3}^{i,i+1}(\mathbf{r}_i\mathbf{v}_i^T + \mathbf{v}_i\mathbf{r}_i^T)\right.$$
$$\left. + T_{3,-3}^{i,i+1}(\mathbf{v}_i\mathbf{v}_i^T)\right] \tag{14a}$$

$$\mathbb{A}_1^i = |\mathbf{v}_i|\left[(T_{0,-1}^{i,i+1} + \epsilon^2 T_{0,-3}^{i,i+1}) + T_{0,-3}^{i,i+1}(\mathbf{r}_i\mathbf{r}_i^T) + T_{1,-3}^{i,i+1}(\mathbf{r}_i\mathbf{v}_i^T + \mathbf{v}_i\mathbf{r}_i^T)\right.$$
$$\left. + T_{2,-3}^{i,i+1}(\mathbf{v}_i\mathbf{v}_i^T)\right] - \mathbb{A}_2^i \tag{14b}$$

We use this formulation to build the following linear system that describes the relation between the velocity along the discrete rod and the force density applied on it:

$$\mathbf{U} = \mathbb{A}\mathbf{F}, \tag{15}$$

where $\mathbf{U} = [\dot{\mathbf{x}}_0, \dot{\mathbf{x}}_1, \ldots, \dot{\mathbf{x}}_{N-1}]^T$ is the velocity vector of the nodes (with no-slip boundary condition, the velocity of one point on the rod is equal to the velocity of viscous fluid at the same point) and $\mathbf{F} = [\mathbf{f}_0, \mathbf{f}_1, \ldots, \mathbf{f}_{N-1}]^T$ is the vector containing the force density at each node. The hydrodynamic force associated with ith node is the product of the force density $\mathbf{f}_i$ and its Voronoi length Δl_i such that

$$\mathbf{F}_i^h = \mathbf{f}_i \Delta l_i. \tag{16}$$

2.3. Contact model

In this subsection, we describe the contact model to enforce non-penetration condition between two approaching edges; this model has been described in sufficient detail in [61]. We first collect all the collision pairs (two edges that intersect) [66]. In our simulation code, a simple brute force method was employed to detect collisions. However, if the number of nodes is too large, e.g., large-scale elastic rod assemblies presented in Ref. [67], the collision detection method can be made efficient by bounding volume hierarchy (BVH) through axis-aligned bounding boxes (AABBs) [68]. Referring to Fig. 4, the spatial coordinates of the ith rod segment, $S_i = (\mathbf{x}_i, \mathbf{x}_{i+1})$, can be extracted from the generalized DOF vector $\mathbf{q}$,
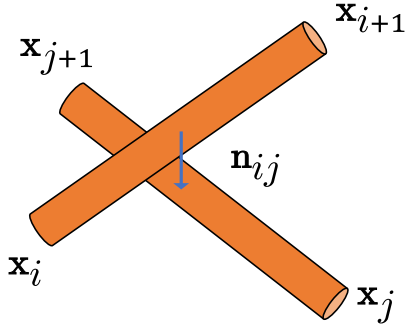
Fig. 4. Notations of contact between two line segments S_i and S_j.

such that we can calculate the minimum Euclidean distance between two rod segments S_i and S_j,

$$\delta_{i,j}^{\min} = \mathrm{md}(\mathbf{x}_i, \mathbf{x}_{i+1}, \mathbf{x}_j, \mathbf{x}_{j+1}). \tag{17}$$

Then the collision detection procedure collects a set of collision pairs (S_i, S_j), with $\delta_{i,j}^{\min} < 2r_0$, where r_0 is the rod radius. The penetration depth $\epsilon_{i,j}$ (should be always positive) of a collision pair (S_i, S_j) is defined as

$$\epsilon_{i,j} = 2r_0 - \delta_{i,j}^{\min}. \tag{18}$$

We are looking for the minimum displacements $\{\Delta\mathbf{x}_i, \Delta\mathbf{x}_{i+1}, \Delta\mathbf{x}_j, \Delta\mathbf{x}_{j+1}\}$ such that the new coordinates define an interference free configuration [69]. Since all the nodes have the same mass in our simulation, the required collision displacement of [61] simplifies to

$$\Delta\mathbf{x}_i = -\frac{1}{2}\mathbf{n}_{ij}w_i \tag{19a}$$

$$\Delta\mathbf{x}_{i+1} = -\frac{1}{2}\mathbf{n}_{ij}(1-w_i) \tag{19b}$$

$$\Delta\mathbf{x}_j = \frac{1}{2}\mathbf{n}_{ij}w_j \tag{19c}$$

$$\Delta\mathbf{x}_{j+1} = \frac{1}{2}\mathbf{n}_{ij}(1-w_j), \tag{19d}$$

where $\mathbf{n}_{ij}$ is the minimum distance vector between S_i and S_j (with $|\mathbf{n}_{ij}| = \delta_{i,j}^{\min}$), and w_i (as well as w_j) is the barycentric coordinate of the contact point on the line segment. For a prescribed collision-based displacement at the ith node, the contact force is

$$\mathbf{F}_i^C = \frac{1}{h^2}\Delta\mathbf{x}_i m_i, \tag{20}$$

where h is the time step size of the time-marching scheme (see next section) and m_i is the lumped mass of the ith node. Similar results can be obtained for $(i+1)$th, jth, and $(j+1)$th nodes.

The contact handling mechanism imposes an upper limit on the time step size of the algorithm in Section 2.4. If the time step size is too large, one edge may pass through another edge in a single time step without any contact being detected. In the results presented in this paper, the time step size is taken to be small enough to avoid this situation. Another option is to employ continuous collision detection [70] and detect possible contacts occurring within a single time step.

2.4. Numerical framework

Now we turn to the overall numerical framework of flagellar bundling simulation that involves updating the configuration of two rods with time. At each time step t_k, we know the DOF vectors and their time derivative (velocity vectors). To march forward in time, we need to compute the hydrodynamic force experienced by elastic rods and then solve the equations of motion, accounting for the contact between two filaments, to get the DOFs and velocities of next time step, $t_{k+1} = t_k + h$ (h is the time step size).

Besides the flow generated by its own hydrodynamic force, the drag force applied on one rod also contributes to a flow field affecting the other one, and vice versa. To account for the interplay between the two, the linear system $\mathbf{U} = \mathbb{A}\mathbf{F}$ in Eq. (15) should be expanded from size of $3N \times 3N$ to $6N \times 6N$,

$$\begin{bmatrix} \mathbf{U}^{(1)} \\ \mathbf{U}^{(2)} \end{bmatrix} = \begin{bmatrix} \mathbb{A}^{(11)} & \mathbb{A}^{(12)} \\ \mathbb{A}^{(21)} & \mathbb{A}^{(22)} \end{bmatrix} \begin{bmatrix} \mathbf{F}^{(1)} \\ \mathbf{F}^{(2)} \end{bmatrix}, \tag{21}$$

where matrices $\mathbb{A}^{(12)}$ and $\mathbb{A}^{(21)}$ show the interaction between two rods in viscous fluid, $\mathbf{F}^{(1)}$, and $\mathbf{F}^{(2)}$ are the $3N$-sized hydrodynamic force density vectors for the two rods, and $\mathbf{U}^{(1)}$, and $\mathbf{U}^{(2)}$ are the velocity vectors of same size. We use LDLT decomposition to obtain the viscous drag forces from the linear system in Eq. (21). LDLT method decomposes a positive-definite matrix into the product of a lower triangular matrix and its conjugate transpose, i.e., $\mathbb{A} = \mathbb{L}\mathbb{D}\mathbb{L}^T$, where $\mathbb{L}$ is a lower unit triangular (unitriangular) matrix and $\mathbb{D}$ is a diagonal matrix. This type of decomposition is useful for efficient numerical solutions.

After computing the hydrodynamic forces acting on the rod, we independently solve for the DOF and velocity vectors of each rod from the equations of motion by a first order, implicit Euler integration,

$$\mathbf{E} \equiv \mathbb{M}\Delta\mathbf{q}(t_{k+1}) - h\mathbf{M}\dot{\mathbf{q}}(t_k) - h^2\left(\mathbf{F}^{\mathrm{int}} + \mathbf{F}^c + \mathbf{F}^h\right) = \mathbf{0}, \tag{22a}$$

$$\mathbf{q}(t_{k+1}) = \mathbf{q}(t_k) + \Delta\mathbf{q}(t_{k+1}), \tag{22b}$$

$$\dot{\mathbf{q}}(t_{k+1}) = \frac{1}{h}\Delta\mathbf{q}(t_{k+1}), \tag{22c}$$

where the DOFs of the previous time step, $\mathbf{q}(t_k)$, and the velocities, $\dot{\mathbf{q}}(t_k)$ are known; the DOFs, $\mathbf{q}(t_{k+1})$, and velocities, $\dot{\mathbf{q}}(t_{k+1})$, of the next time step need to be solved for; $\mathbf{F}^{\mathrm{int}}$ is the internal elastic force of size $(4N-1)$ computed from Eq. (6); $\mathbf{F}^h$ is the hydrodynamic force computed from Eq. (21) and Eq. (16); $\mathbf{F}^c$ is the contact force in Eq. (20); and $\mathbb{M}$ is the diagonal mass matrix comprised of lumped masses. The Jacobian associated with Eq. (22) is necessary for Newton's iteration and can be expressed as

$$\mathbb{J} = \mathbf{M} - h^2\left[-\frac{\partial^2(E_s + E_b + E_t)}{\partial\mathbf{q}^2}\right]. \tag{23}$$

Here, the gradient of the hydrodynamic force and contact forces cannot be analytically evaluated, i.e. external forces are treated explicitly.

At the beginning of each time step, we initialize the external contact force $\mathbf{F}^c$ as zeros, and compute the hydrodynamic force by Eq. (21) and Eq. (16), then solve the equations of motion in Eq. (22) to update the DOFs. This DOF is used to detect any collision. If the non-penetration condition is broken, external contact forces are updated on the basis of Eqs. (19) and (20) and the equations of motion in Eq. (22) are solved again. This rewind and re-solve process continues until the non-penetration condition is achieved for every segment pair. The overall algorithm of flagellar bundling simulation can be found in Appendix A.
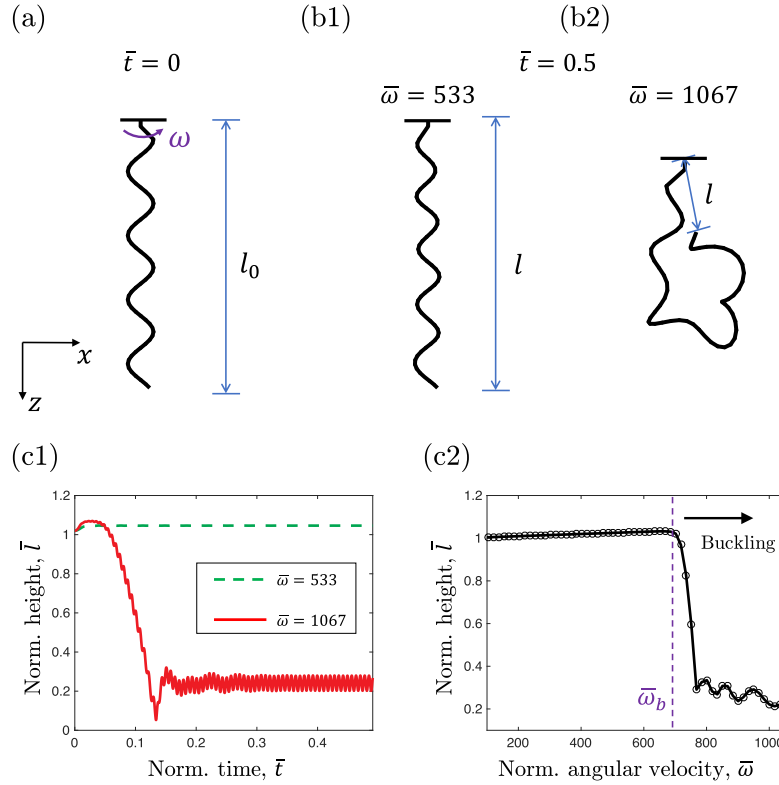
Fig. 5. (a) The helical rod in stress free configuration. (b) Configuration of rotating flagellum at (b1) stable phase (with $\bar{\omega} = 533$) and (b2) buckling instability phase (with $\bar{\omega} = 1067$). (c1) Normalized height $\bar{l}$ as a function of normalized time for a single helical rod rotating at $\bar{\omega} \in \{533, 1067\}$. (c2) Normalized height $\bar{l}$ as a function of normalized angular velocity $\bar{\omega}$ for the definition of critical buckling angular velocity $\bar{\omega}_b$.

3. Flagellar buckling instability

A helical filament rotating in a viscous fluid would undergo buckling instability when its angular velocity exceeds a threshold value [38,43,45]. Here, we discuss the buckling behavior of a single rotating helix in a viscous medium, for comparison between the DER-LSBT model, that shows reasonable agreement with macroscale experiment [38,43], and the newly introduced DER-RSS framework. We first provide specifics on the geometric and physical parameters of the numerical study; these parameters correspond to macroscopic experiments [38,43]. However, we will present our simulation results in non-dimensional form. We assume a right-handed helical rod, made out of a linear elastic material, with Young's modulus $E = 10\text{MPa}$ and Poisson's ratio $\nu = 0.5$ (incompressible). The rod density, $\rho = 1000\text{kg/m}^3$, is assumed to be equal to the fluid density so that no buoyant force is present. Radius of circular cross section is $r_0 = 1\text{mm}$, (and, therefore, second moment of inertia, $I = \pi r_0^4/4$, and cross section area, $A = \pi r_0^2$). The fluid viscosity is $\mu = 1.0\text{Pa} \cdot \text{s}$. As shown schematically in Fig. 5(a), in the stress free configuration, the first edge, $\mathbf{e}^0$, connecting $\mathbf{x}_0$ and $\mathbf{x}_1$, is parallel to the z-axis; the second edge connecting $\mathbf{x}_1$ and $\mathbf{x}_2$ is $\mathbf{e}^1 = R\hat{z} + R\hat{x}$ ($\hat{x}$ and $\hat{z}$ are unit vectors along the x and z axes, respectively); all other nodes, $[\mathbf{x}_3, \mathbf{x}_4, \ldots, \mathbf{x}_{N-1}]$, fall on a helical shape. The helical configuration in the current numerical study (axis length $l_0 = 0.2\text{m}$, helical pitch $\lambda = 5\text{cm}$, and helical radius $R = 1\text{cm}$), similar to the previous explorations [38,43], is in the biologically relevant regime [34]. The rotating angular velocity is $\omega \in \{0, 50\}\text{rpm}$, such that the Reynolds number in our numerical study is $\rho\omega Rr_0/\mu \leq 4 \times 10^{-2}$, i.e. always in the Stokes limit [43,45]. We then discuss the boundary conditions. The helical filament immersed in an unbounded fluid is clamped at one extremity, with first two nodes ($\mathbf{x}_0$ and $\mathbf{x}_1$) fixed. The first twisting an-

gle, θ^0, is rotated anticlockwise (viewed from above with a prescribed angular velocity, ω). Apart from these fixed DOFs, all other nodes and edges are free and evolve based on the balance between elastic and fluid forces. In this representative setup, the number of nodes along the discrete rod is $N = 65$, corresponding to a Voronoi length of $\Delta l_i = 5\text{mm}$. The regularization parameter ϵ in RSS theory is related to the rod radius r_0, and can be determined based on the drag force experienced by a finite cylinder moving in viscous fluid perpendicularly to its axis. The regularization parameter, ϵ, varies slightly with the length of each edge. In our simulations, we choose $\epsilon = 1.02r_0$ based on the value of $\Delta l_i/r_0$ [51]. The time step size in this simulation is $h = 1\text{ms}$. Details of the convergence study on space and time discretization can be found in Appendix B. We also briefly review the LSBT, and compare the numerical results performed by DER-LSBT method and DER-RSS framework in Appendix C.

In Fig. 5(b1-b2), we present two representative deformed shapes of the rod rotating at two different normalized angular velocities, $\bar{\omega} \in \{533, 1067\}$, at $\bar{t} = 0.5$. Notice that, due to the slender geometry of the system, bending is the prominent mode of the deformation of a rod, such that the angular velocity and the time are normalized by Jawed and Reis [43],

$$\bar{\omega} = \omega\mu l_0^4/(EI), \tag{24a}$$

$$\bar{t} = t(EI)/\mu l_0^4. \tag{24b}$$

When the helical rod rotates at a lower angular velocity, e.g. $\bar{\omega} = 533$, the whole structure retains its helical shape and stretches a little due to the hydrodynamic force from viscous fluid, seeing Fig. 5(b1); however, when the helical rod spins at a higher frequency, e.g. $\bar{\omega} = 1067$, the structure undergoes buckling instabil-
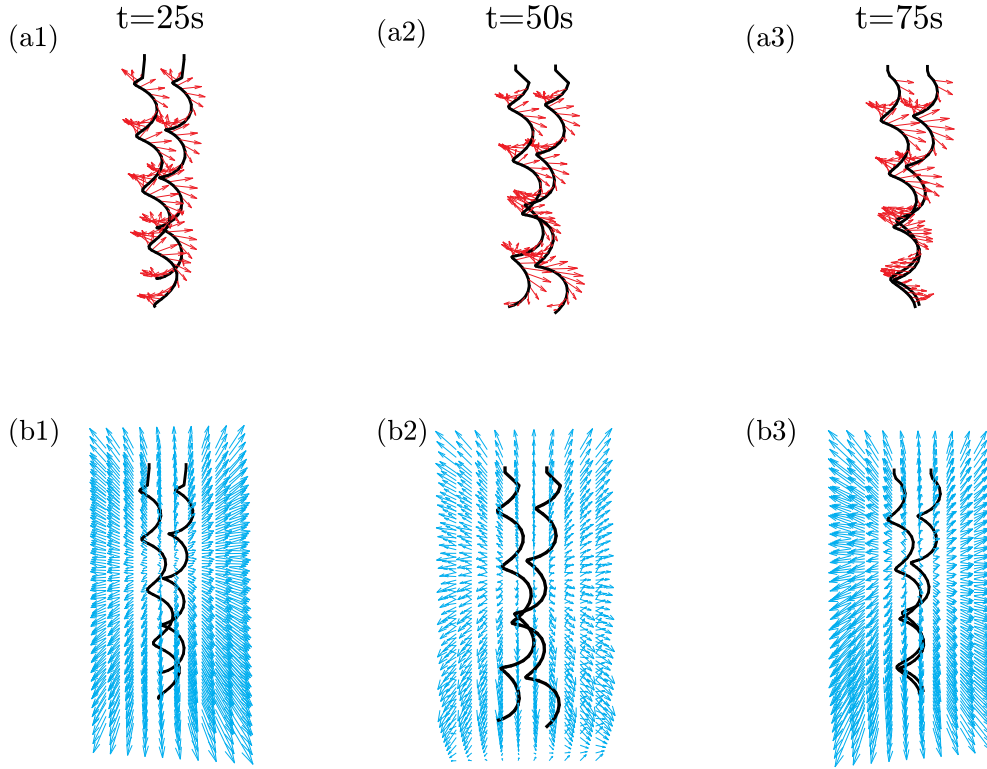
Fig. 6. (a1)-(a3) Hydrodynamic force applied on soft filaments at different time step, $t \in \{25, 50, 75\}$s. (b1)-(b3) Flow field around two helical rods at different time step, $t \in \{25, 50, 75\}$s. The physical parameters and boundary setup are identical to Fig. 1.

ity and, in Fig. 5(b2), deforms into a highly nonlinear configuration [38,43,45]. We consider the end to end length, l, to quantify the deformation of a helical rod. In Fig. 5(c1), we plot the normalized height of helical rod, $\bar{l} = l/l_0$, as a function of time for two different normalized angular velocity $\bar{\omega} \in \{533, 1067\}$. The final steady-state configurations can be achieved after $\bar{t} = 0.3$ for both these two cases.

Based on the previous investigations of our own [38,43,45], there exists a critical buckling angular velocity above which the final configuration is distorted, similar to the one shown in Fig. 5(b2). We perform a parameter sweep along angular velocity to find the critical buckling angular velocity, $\bar{\omega}_b$, of a single helical rod rotating in a low Reynolds fluid. Fig. 5(c2) shows the normalized end to end length, $\bar{l}$, at time $\bar{t} = 1.0$, as a function of normalized angular velocity, $\bar{\omega}$. As expected, the soft filament remains in stable regime and stretch as a linear function of $\bar{\omega}$ at low enough angular velocity; When $\bar{\omega}$ is larger than a critical value, the rod will undergo buckling instability and deform into a curved shape. The maximum normalized angular velocity that retains the helical shape of the structure is defined as the critical buckling angular velocity, $\bar{\omega}_b$. For the specific geometry chosen in this study, the normalized critical angular velocity is $\bar{\omega}_b \approx 675$. The critical buckling angular velocity captured by LSBT is similar to the one reported by RSS, with relative error less than 5%, which demonstrates the correctness and accuracy of the coupling framework between DER and RSS, seeing Appendix C. The experimental validation of the presented DER-RSS is in Appendix D.

4. Flagellar bundling

We now turn to the main contribution of the current study and include the effect of the interaction between two rotating helical rods in a viscous fluid. Previous coupling numerical framework be-

tween DER and LSBT can also capture the buckling instability of a single helical rod rotating in viscous fluid (details in Appendix C) [38,43,45], but meets numerical issue when applied to study the bundling behavior of multiple flagella. LSBT divides the hydrodynamic force generated by soft filaments into two parts – local (dipoles) and nonlocal terms (Stokeslets). As two rod segments attract each other and become closer, one rod may enter the "local" regime of the other rod. This often results in ill-conditioned problems in Eq. (C.3). This issue, on the other hand, can be solved by RSS method, for its continuous evaluation of Stokeslet generated by cylinder segment.

Figure 1 shows a sequence of snapshots of two helices (axis length $l_0 = 0.2$m, normalized helical pitch $\lambda/l_0 = 0.25$, and normalized helical radius $R/l_0 = 0.05$) rotating side by side with same frequency, $\bar{\omega} = 320$ (both anticlockwise when viewed from above), at a normalized initial distance $\Delta_t/R = 3$. The induced flows of helical rods cause large deflections, and then a bundle form appears. The helices wrap around each other in a right-handed sense; the flow field generated by each helix tilts the other helix, causing the helices to roll around each other and form a right-handed wrapping. We use the end to end distance between the two rods along the x-axis, denoted as Δ_b (see Fig. 1(a1)), as a shape parameter to quantify the bundling behavior between two rotating filaments. This parameter, Δ_b, becomes negative when two rods wrap around each other. The hydrodynamic force as well as the flow generated by helical rods at different time steps, $t \in \{25, 50, 75\}$s are in Fig. 6. Notice that the hydrodynamic force is computed from the velocity of helical rods, referring to Eq. (21); then the flow field at a given point, $\hat{\mathbf{x}}$, can be easily derived based on Eq. (9) [71].

We first examine the effect of angular velocity on the end to end distance. Fig. 7(a1)-(a3) shows the trajectory of the ends of the rods – the last node in DER simulation – on the $x - y$ plane at three different normalized angular velocities $\bar{\omega} \in \{43, 107, 427\}$,
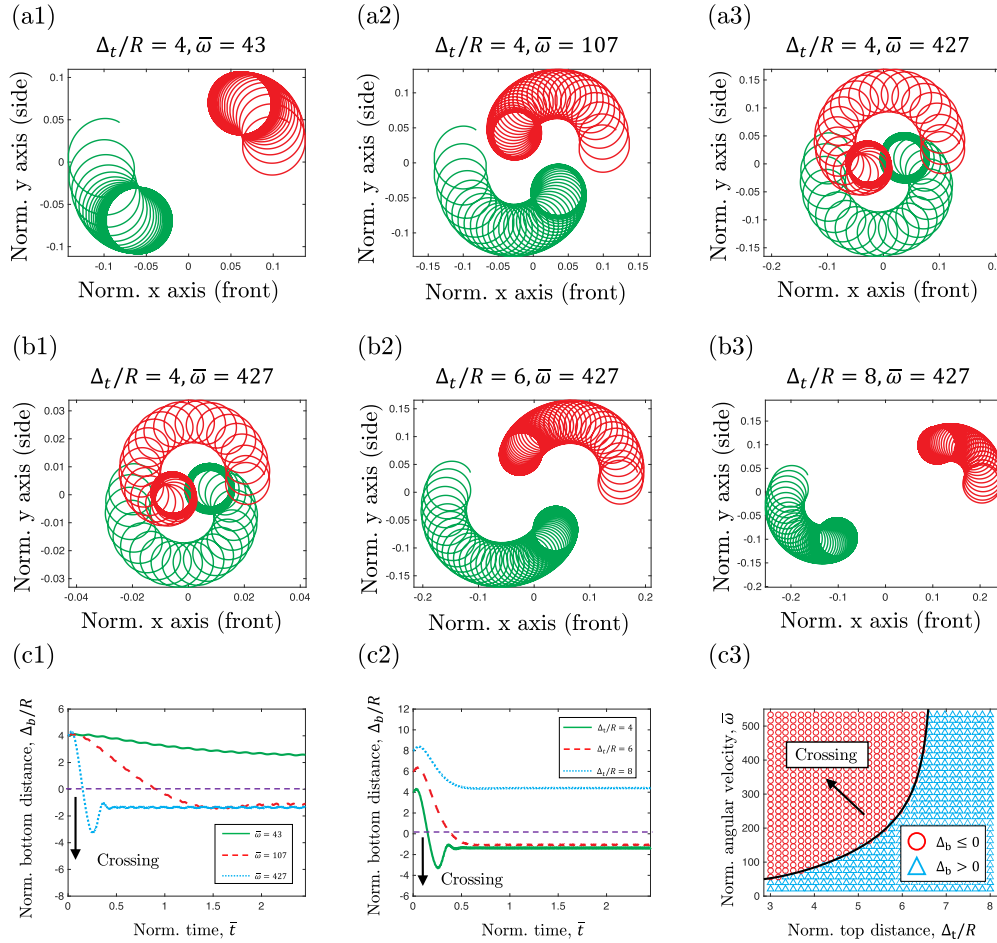
Fig. 7. Projected trajectory of helical end point on normalized $x-y$ plane, with different parameter combinations: (a) normalized top distance $\Delta_t/R = 4$ fixed, varying angular velocity $\bar{\omega} \in \{43, 107, 427\}$; (b) normalized angular velocity $\bar{\omega} = 427$ fixed, varying initial top distance $\Delta_t/R \in \{4, 6, 8\}$. Normalized bottom distance Δ_b/R as a function of normalized time by varying (c1) angular velocity $\bar{\omega}$ and (c2) initial top distance Δ_t/R. (c3) Phase diagram of the critical crossing angular velocity in the $(\Delta_t/R, \bar{\omega})$ parameter space.

with the normalized top distance fixed at $\Delta_t/R = 4$. Here, the x axis (as well as y axis) is normalized by the helical axis length l_0, $\bar{x} = x/l_0$. Similar setup from macroscopic model experiments can be found in [21]. We observe that the two flagella come closer through a U-shaped trajectory of the last node. Eventually, the two ends settle to a steady circular path. Fig. 7(c1) plots the normalized end to end distance, Δ_b/R, as a function of time, in all these three cases. While the top distance, Δ_t, – the distance between the first nodes on two rods – remains fixed with time due to the boundary conditions imposed in the simulation, the end to end distance varies significantly due to the deformation from hydrodynamic forces. Note that $\Delta_t = \Delta_b$ at time $\bar{t} = 0$. For small angular velocity, two rods will become closer in their final stable shapes with $0 < \Delta_b/R < \Delta_t/R$, shown in Fig. 7(a1). However, when rotating at a higher angular velocity, two helical rods can go beyond each other, such that a *crossed* configuration with $\Delta_b/R < 0 < \Delta_t/R$ can be achieved, when looking on the $x-z$ plane. An example configuration is presented in Fig. 1(a3).

We next explore the role of the initial top distance, Δ_t, on the bundling behavior of two flagella. In Fig. 7(b1)-(b3), we plot the trajectory of the last nodes of the rods at three different values of top distance, $\Delta_t/R \in \{4, 6, 8\}$, while keeping the normalized angular velocity fixed at $\bar{\omega} = 427$. Fig. 7(c2) shows the end to end distance as a function of scaled time in these three cases. When the top distance is small ($\Delta_t/R = 4$ and $\Delta_t/R = 6$), the crossed shape is achieved within $\bar{t} = 2$. However, in the long distance case

($\Delta_t/R = 8$), the end to end distance eventually reaches a value equal to approximately half of the top distance and always remains positive ($\Delta_b/R > 0$).

To combine all the information together, in Fig. 7(c3), we perform a two dimensional parameter sweep, by varying both angular velocity, $\bar{\omega} \in [0.0, 550.0]$, and initial distance, $\Delta_t/R \in [3.0, 8.0]$, and show the final shape. A circular symbol presents a crossed configuration ($\Delta_b \leq 0$), whereas a triangle stands for $\Delta_b > 0$. The critical normalized angular velocity beyond which this crossed configuration is achieved is defined as $\bar{\omega}_c$, and, in Fig. 7(c3), is indicated by a solid line. This threshold parameter, $\bar{\omega}_c$, first increases as the initial distance Δ_t increases. When the initial distance exceeds $\Delta_t/R \approx 7$, the crossing behavior cannot be achieved even when the angular velocity goes beyond the critical buckling angular velocity, $\bar{\omega}_b$, discussed in the previous section.

Then, we focus on the propulsive force of two helical flagella rotating side by side. The first two nodes are fixed in place and the reaction forces corresponding to this boundary condition (equal to the sum of elastic and external forces on the node in question) can be computed from the simulation. The propulsive force defined here is the sum of the reaction forces applied on the fixed nodes of the two helical filamentary system projected along the z-axis,

$$F_p = \left[(\mathbf{F}_0^{\text{cons}})^{(1)} + (\mathbf{F}_1^{\text{cons}})^{(1)} + (\mathbf{F}_0^{\text{cons}})^{(2)} + (\mathbf{F}_1^{\text{cons}})^{(2)} \right] \cdot \mathbf{n}_z,$$

$$(25)$$
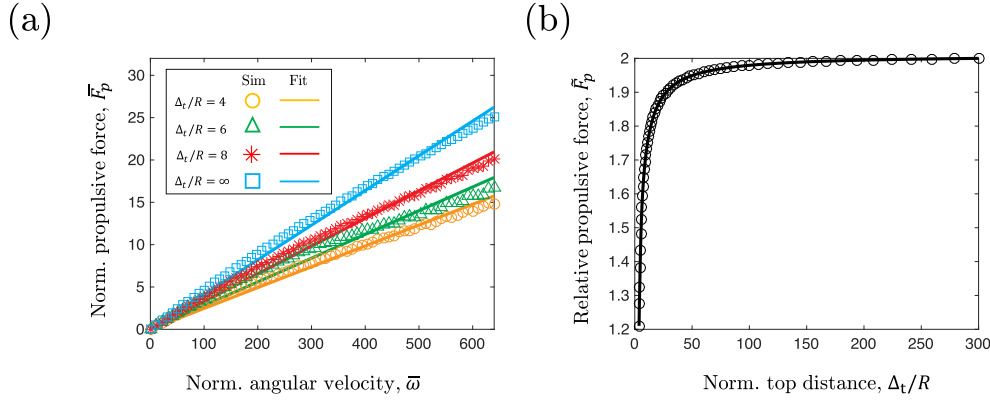
Fig. 8. (a) Normalized propulsive force $\bar{F}_p$ as a function of normalized angular velocity $\bar{\omega}$, by varying normalized top distance, $\Delta_t/R \in \{4, 6, 8, \infty\}$, from simulation (symbols) and linear fit (solid lines). (b) Relative propulsion, $\tilde{F}_p$, as a function of normalized top distance, Δ_t/R, with a fixed normalized angular velocity $\bar{\omega} = 213$.
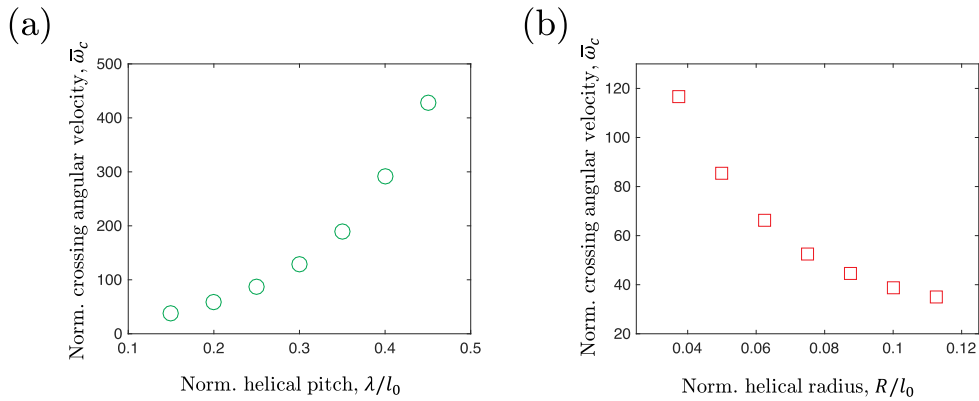
Fig. 9. Normalized critical crossing angular $\bar{\omega}_c$ versus (a1) normalized helical pitch λ/l_0 (with $R/l_0 = 0.05$ and $\Delta_t/R = 4$ fixed) and (a2) normalized helical radius R/l_0 (with $\lambda/l_0 = 0.25$ and $\Delta_t/R = 4$ fixed).

where $\mathbf{n}_z = [0, 0, 1]^T$ is the unit vector along the z-axis, $\mathbf{F}_i^{\mathrm{cons}}$ is the constrained force applied on the ith node, and the superscript represents the rod number. Next, we formulate a non-dimensional propulsive force,

$$\bar{F}_p = F_p l_0^2 / (EI), \tag{26}$$

by normalizing F_p with the characteristic bending force, EI/l_0^2 [43]. In Fig. 8(a), we plot the normalized propulsive force, $\bar{F}_p$, as a function of normalized angular velocity, $\bar{\omega}$, at different values of normalized top distance, $\Delta_t/R \in \{4, 6, 8, \infty\}$. The propulsive force approximately linearly goes up with the increase of the angular velocity in the pre-buckling phase. The propulsive force is maximum when two helices are rotating at infinite distance, i.e. there is no hydrodynamic interaction between the two. As the top distance decreases, the propulsive force monotonically decreases. Compared with the case of $\Delta_t = \infty$, the propulsive force at $\Delta_t/R = 4, 6$, and 8 decreased 40.0%, 31.7%, and 20.2%, respectively. Moreover, in Fig. 8(b), we evaluate the relative propulsive efficiency as a function of normalized top distance, Δ_t/R, with a fixed normalized angular velocity, $\bar{\omega} = 213$. Here, the sum propulsion of two rotating helical system is scaled by the propulsive force of a single rotating filament, $\tilde{F}_p = F_p/F_p^{\mathrm{single}}$; notice that $\tilde{F}_p = 2$ at $\Delta_t = \infty$, i.e. the propulsive force is double when there is no hydrodynamic interaction between two flagella. We clearly see that the propulsive force increases by more than 60% from $\Delta_t/R = 3$ to $\Delta_t/R = 50$, and shows almost no variation beyond $\Delta_t/R > 100$. Regardless of the top distance, the propulsive force with hydrodynamic interaction is always lower than the force without this interaction.

This far, we kept the geometry of the flagella at the representative value. Now, we employ our numerical simulation to explore the effect of the geometric parameters on the critical crossing angular velocity, ω_c, in biologically relevant regime [34]. Specifically, we varied the helical pitch, λ/l_0, and helical radius, R/l_0, to understand the hydrodynamic performances of helices in different shapes. In Fig. 9(a), we vary the normalized helical pitch, $\lambda/l_0 \in [0.15, 0.45]$, at fixed values of radius ($R/l_0 = 0.05$) and top distance ($\Delta_t/R = 4$), and plot the normalized critical crossing angular velocity, $\bar{\omega}_c$, as a function of the normalized helical pitch. Note that the parameter, $\bar{\omega}_c$, strongly depends on the pitch of the flagella. On the other side, we vary helical radius in the range $R/l_0 \in [0.0375, 0.1125]$, at fixed values of $\lambda/l_0 = 0.25$ and $\Delta_t/R = 4$, and, in Fig. 9(b), explore the variation of $\bar{\omega}_c$ with the nondimensional helical radius, R/l_0. We again observe that the helical radius significantly changes the bundling behavior. As the radius increases, the angular velocity required for the crossed configuration decreases. Altogether, these results emphasize the prominent role of geometry of the helical filaments on their hydrodynamic interactions between each other with a focus on biologically relevant regime [34,72]. Our investigation opens up questions on how microorganisms utilize bundling of their flagellar during their motion in low Reynolds environment.

5. Conclusion

We have introduced a computational framework to study the geometrically nonlinear interaction between two neighboring elas-

tic flagella rotating in a viscous fluid. For this purpose, our numerical approach combined DER, RSS, and a contact model. We first studied the mechanical response of a single helical rod undergoing rotation in a low Reynolds environment, and compared the results against the experimentally validated fluid-structure interaction model, LSBT. The relative $\leq 5\%$ error between the critical buckling angular velocity computed from LSBT and the one obtained by RSS indicates the accuracy of the numerical method coupling DER and RSS. Empowered by this simulation tool, we next investigated the dynamics between two rotating soft filaments side-by-side in a viscous fluid. Two rotating helical rods attract each other and become closer because of the coupling flow field generated by each other; and the crossing behavior is related to their initial distance and rotating frequency. The propulsive force, on the other hand, shows a decreasing tendency as two flagella are brought closer to one another. In order to realize the importance of the helical geometry in the propulsion of natural bacterial flagella, the simulation tool was then employed to sweep through parameter space along two geometric parameters (helix pitch and radius), for quantification of the bundling behavior and the critical rotating velocity for crossing. Our findings are scale invariant and can be applied to bacterial propulsion at micron-scale as long as the dimensionless groups (e.g. Reynolds number, normalized angular velocity, normalized helical pitch, and so on) are maintained. The results on the effect of angular velocity and geometry on the bundling behavior and propulsive force are, therefore, potentially relevant to flagellated bacteria.

The significant effect of flagellum geometry, flexibility, and the interaction in viscous fluid poses a nontrivial design space for both nature and engineering. This might have potential application in controlling the swimming speed and direction in multiflagellated microorganisms. Our findings may also provide guidelines for the design of laboratory experiments on bacterial propulsion and biomimetic soft robots. Since we avoid the numerical discontinuity in previous long-range hydrodynamic force model, LSBT, our framework can be directly applied for the simulations of bacterial system with more than one flagellum. The sparse space discretization of RSS shows a better computational efficiency than LSBT, and this fast numerical framework can be treated as a data generator by sweeping the essential geometric and physical parameters, for a better understanding of biophysics in natural environment, and can also be potentially used for the optimized design and online control of multi-flagellated soft robots. We hope that our numerical investigations can motivate a fundamental understanding of the biophysics of microorganisms, as well as support modeling, design, and control of functional soft robots.

Declaration of Competing Interest

The authors declare that they have no known competing financial interests or personal relationships that could have appeared to influence the work reported in this paper.

CRediT authorship contribution statement

Weicheng Huang: Conceptualization, Methodology, Software, Validation, Investigation, Writing - original draft. **M. Khalid Jawed:** Conceptualization, Software, Writing - review & editing, Supervision, Funding acquisition.

Acknowledgments

Appendix A. Flagellar bundling simulation process

In Algorithm 1, we provide a pseudo code of flagellar bundling simulation.

Appendix B. Convergence Study

In this Appendix, we present a convergence study with both time and space discretization for the coupling framework between DER and RSS. In Fig. B.10(a), we show the relationship between the normalized height, $\bar{l}$, and the normalized angular velocity $\bar{\omega}$, at different values of number of vertices, $N \in \{43, 65, 81\}$, with a fixed time step size, $h = 1$ms. In the simulations presented in Fig. B.10(a), we kept the regularization parameter fixed at $\epsilon = 1.02r_0$. According to RSS theory, this parameter ϵ may vary between $1.01r_0$ to $1.04r_0$ as N is changed. However, the effect of 3% variation in ϵ has negligible effect on the simulation results.

We use a similar plot in Fig. B.10(b) to show the convergence with time discretization for this numerical framework, at $N = 65$. The simulation results remain the same when the time step size, h, is varied from $1e^{-3}$ to $1e^{-4}$.

Appendix C. Comparison between LSBT and RSS

We briefly review the Lighthill Slender Body Theory (LSBT) and compare with Regularized Stokeslets Segments (RSS) method in this section.

LSBT assumes a series of Stokeslets and dipoles along the centerline of rod, and build a relationship between the velocity field contributed by flagellum with the hydrodynamic force applied on it. The continuous formulation of LSBT is [38,43,45]

$$\mathbf{u}(s) = \frac{\mathbf{f}_\perp(s)}{4\pi\mu} + \int_{|\mathbf{r}(s',s)|>\delta} \mathbf{f}(s') \cdot \mathbb{J}(\mathbf{r})ds', \tag{C.1}$$

where s is the arclength parameter of the rod, $\mathbf{f}_\perp(s) = \mathbf{f}(s)[\mathbb{I} - \mathbf{t}(s) \otimes \mathbf{t}(s)]$ is the component of $\mathbf{f}(s)$ in the plane perpendicular to the tangent $\mathbf{t}(s)$, $\mathbf{r}(s', s)$ is the position vector from s' to s, $\delta = r_0\sqrt{e}/2$ (r_0 is the rod radius and e is the Napier's constant), and $\mathbb{J}(\mathbf{r}) = \frac{1}{8\pi\mu}(\frac{\mathbb{I}}{|\mathbf{r}|} + \frac{\mathbf{r}\mathbf{r}^T}{|\mathbf{r}|^3})$ is the Oseen tensor.

We then use a discrete version of Eq. (C.1) to relate the velocity $\mathbf{u}(q)$ at node q with the force $\mathbf{f}(p)$ on node p, [38,43,45]

$$\mathbf{u}(q) = \frac{\mathbf{f}_\perp(q)}{4\pi\mu\Delta} + \sum_{p=0, p\neq q}^{N-1} \frac{1}{8\pi\mu|\mathbf{r}|}\left[\mathbb{I} + \frac{\mathbf{r}\mathbf{r}^T}{|\mathbf{r}|^2}\right]\mathbf{f}(p), \tag{C.2}$$

where $\Delta = 2\delta$ is the edge length in the discrete rod. This relationship between forces and velocities is similar to Regularized Stokeslets Segments theory, and can be written as a linear system of size $3N$,

$$\mathbf{U} = \mathbb{A}\mathbf{F}. \tag{C.3}$$

Note that for the specific helix discussed in this paper (axis length $l_0 = 0.2$m, helical pitch $\lambda = 5$cm, helical radius $R = 1$cm, arclength $L = 0.32$m, and rod radius $r_0 = 1$mm), edge length should be $\Delta = 1.65$mm, resulting into $N = 195$ nodes.

In Fig. C.11(a), we plot the normalized height, $\bar{l}$, as a function of normalized rotating velocity $\bar{\omega}$, with two different fluid-structure interaction models: LSBT and RSS. The critical angular velocity obtained by LSBT is $\bar{\omega}_b^{\text{LSBT}} \approx 660$, and the one achieved by RSS is $\bar{\omega}_b^{\text{RSS}} \approx 675$, with relative error less than 5%.

Regarding computational efficiency, note that the size of each edge is fixed at Δ in LSBT. If the rod too slender (i.e. ratio between the total arclength and cross-sectional radius is large), we would require too many vertices and, consequently, a longer computational time. On the other hand, RSS allows more aggressive discretization (i.e. lower number of nodes). In Fig. C.11(b), we show
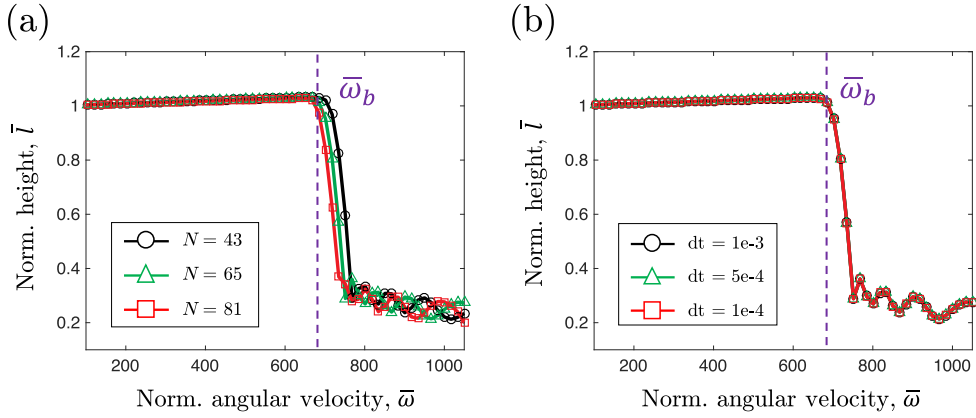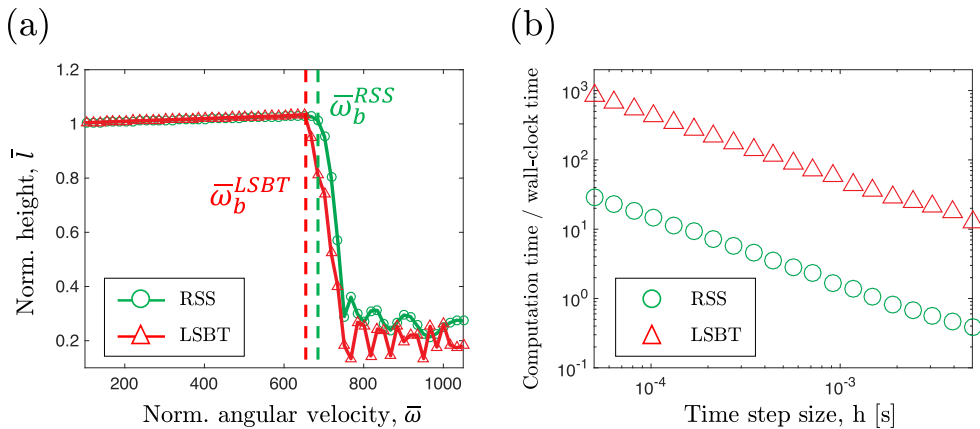
Fig. B.10. Convergence study for (a) space discretization and (b) time discretization.

the computational time, normalized by the wall-clock time, as a function of time step size, h, for both RSS ($N = 65$) and LSBT ($N = 195$) method. The simulations ran on a single thread of AMD Ryzen 1950X CPU @ 3.4 GHz. Even though the node number of LSBT is only three times larger than RSS, the computational time of LSBT is almost 30 times slower than the time performed by RSS. This is rooted in the computational time of solving the dense linear system in Eq. (15) and Eq. (C.3). On the other side, the computational time for Fig. 1 is approximately 8 times larger than the wall-clock time when the time step size is set to be $h = 1$ms.

Appendix D. Validation of DER-RSS method

In this section, we compare the DER-RSS framework against previous experimental data. The experimental data is available in Fig. 4(b) and (c) of Ref. [38]. The physical parameters used in the numerical approach are: Young's modulus $E = 1.255$MPa, fluid viscosity is $\mu = 1.6$Pa · s, rod radius $r_0 = 1.58$mm, helical axis length $l_0 = 20.00$cm, helical pitch $\lambda = 5.00$cm, helical radius $R = 1.59$cm, which are identical to the experimental setup in Ref. [38]. In Fig. D.12(a) and (b), we plot the dependence of critical buckling angular velocity, $\bar{\omega}_b$, on helical pitch and helical radius. Excellent agreements between the DER-RSS algorithm and experimental data indicate the correctness and accuracy of present numerical framework.
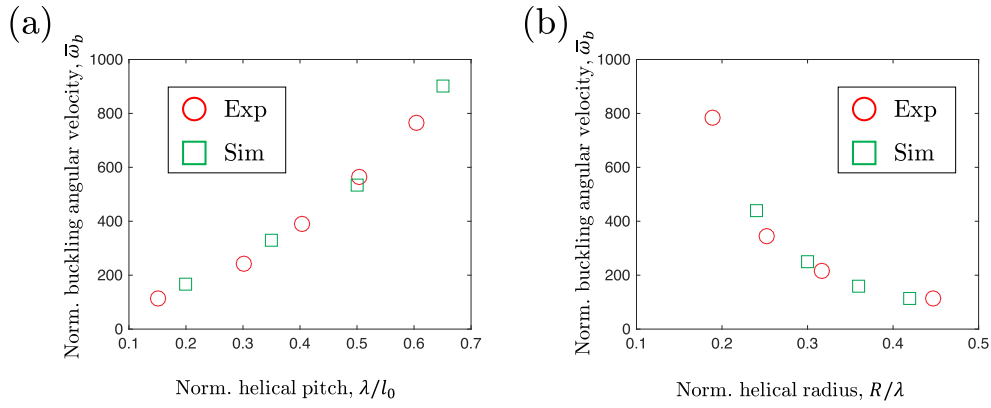
Appendix E. Video

We provide a video corresponding to Fig. 1 of the main manuscript as supplementary material.

Supplementary material

Supplementary material associated with this article can be found, in the online version, at doi:10.1016/j.compfluid.2021.105038.

References

[1] Leifson E, Cosenza B, Murchelano R, Cleverdon R. Motile marine bacteria I.: techniques, ecology, and general characteristics. J Bacteriol 1964;87(3):652–66.
[2] Purcell EM. The efficiency of propulsion by a rotating flagellum. Proc Natl Acad Sci 1997;94(21):11307–11.
[3] Vogel R, Stark H. Motor-driven bacterial flagella and buckling instabilities. Eur Phys J E 2012;35(2):15.
[4] Berg HC. Cell motility: turning failure into function. Nat Phys 2013;9(8):460.
[5] Park Y, Kim Y, Ko W, Lim S. Instabilities of a rotating helical rod in a viscous fluid. Phys Rev E 2017;95(2):022410.
[6] Son K, Guasto JS, Stocker R. Bacteria can exploit a flagellar buckling instability to change direction. Nat Phys 2013;9(8):494.
[7] Macnab RM, Ornston MK. Normal-to-curly flagellar transitions and their role in bacterial tumbling. stabilization of an alternative quaternary structure by mechanical force. J Mol Biol 1977;112(1):1–30.
[8] Calladine C. Construction of bacterial flagella. Nature 1975;255(5504):121.
[9] Darnton NC, Berg HC. Force-extension measurements on bacterial flagella: triggering polymorphic transformations. Biophys J 2007;92(6):2230–6.
[10] Flores H, Lobaton E, Méndez-Diez S, Tlupova S, Cortez R. A study of bacterial flagellar bundling. Bull Math Biol 2005;67(1):137–68.

Fig. C.11. (a) Normalized height $\bar{l}$ as a function of normalized angular velocity $\bar{\omega}$ for LSBT and RSS. (b) The ratio between computational time and wall-clock time as a function of time step size h for LSBT and RSS.

Fig. D.12. Normalized critical buckling angular, $\bar{\omega}_b$, versus (a1) normalized helical pitch λ/l_0 (with $l_0 = 20.00$cm and $R = 1.59$cm fixed) and (a2) normalized helical radius R/λ (with $l_0 = 20.00$cm and $\lambda = 5.00$cm fixed).

Algorithm 1 Flagellar bundling simulation.

Input: $k \leftarrow 0$, $t_k \leftarrow 0.0$s, N, r_0, $l \in \{1, 2\}$, $\mathbf{q}^{(l)}(t_k)$, $\dot{\mathbf{q}}^{(l)}(t_k)$, ω, h, T, tol

while $t_k \leq T$ **do**
  $t_{k+1} = t_k + h$
  for $l = 1$ to $l = 2$ **do**
    $\left(\theta^0\right)^{(l)} \leftarrow \left(\theta^0\right)^{(l)} + h\omega$
    $(\mathbf{F}^c)^{(l)} \leftarrow \mathbf{0}$
  end for
  Calculate $\mathbb{A}^{(11)}, \mathbb{A}^{(12)}, \mathbb{A}^{(21)}$, and $\mathbb{A}^{(22)}$ from Eq. (14)
  Calculate $(\mathbf{F}^h)^{(1)}$ and $(\mathbf{F}^h)^{(2)}$ from Eqs. (21) and (16)
  solved $\leftarrow 0$
  while solved $== 0$ **do**
    for $l = 1$ to $l = 2$ **do**
      $n \leftarrow 0$
      Guess $\mathbf{q}_n^{(l)}(t_{k+1}) = \mathbf{q}^{(l)}(t_k) + h\dot{\mathbf{q}}^{(l)}(t_k)$
      $error \leftarrow 10 \times tol$
      while $error > tol$ **do**
        Compute $\mathbf{E}_n^{(l)}$ in Eq. (22) and $\mathbb{J}_n^{(l)}$ in Eq. (23)
        $\mathbf{q}_{n+1}^{(l)}(t_{k+1}) = \mathbf{q}_n^{(l)}(t_{k+1}) - \mathbb{J}_n^{(l)} \backslash \mathbf{E}_n^{(l)}$
        $n \leftarrow n + 1$
        $tol = |\mathbf{E}_n^{(l)}|$
      end while
    end for
    solved $\leftarrow 1$
    for $i = 0$ to $i = N - 2$ **do**
      for $j = 0$ to $j = N - 2$ **do**
        Compute $\delta_{i,j}^{\min}$ from Eq. (19)
        if $\delta_{i,j}^{\min} < 2r_0$ **then**
          Compute $(\mathbf{F}_i^c)^{(1)}$, $(\mathbf{F}_{i+1}^c)^{(1)}$, $(\mathbf{F}_j^c)^{(2)}$, and $(\mathbf{F}_{j+1}^c)^{(2)}$
          from Eq. (20)
          solved $\leftarrow 0$
        end if
      end for
    end for
  end while
  $k \leftarrow k + 1$
end while

[11] Cisneros LH, Kessler JO, Ortiz R, Cortez R, Bees MA. Unexpected bipolar flagellar arrangements and long-range flows driven by bacteria near solid boundaries. Phys Rev Lett 2008;101(16):168102.

[12] Brown MT, Steel BC, Silvestrin C, Wilkinson DA, Delalez NJ, Lumb CN, et al. Flagellar hook flexibility is essential for bundle formation in swimming escherichia coli cells. J Bacteriol 2012;194(13):3495–501.

[13] Hyon Y, Powers TR, Stocker R, Fu HC, et al. The wiggling trajectories of bacteria. J Fluid Mech 2012;705:58–76.

[14] Reigh SY, Winkler RG, Gompper G. Synchronization and bundling of anchored bacterial flagella. Soft Matter 2012;8(16):4363–72.

[15] Maniyeri R, Kang S. Numerical study on bacterial flagellar bundling and tumbling in a viscous fluid using an immersed boundary method. Appl Math Model 2014;38(14):3567–90.

[16] Hintsche M, Waljor V, Großmann R, Kühn MJ, Thormann KM, Peruani F, et al. A polar bundle of flagella can drive bacterial swimming by pushing, pulling, or coiling around the cell body. Sci Rep 2017;7(1):16771.

[17] Nguyen FT, Graham MD. Impacts of multiflagellarity on stability and speed of bacterial locomotion. Phys Rev E 2018;98(4):042419.

[18] Constantino MA, Jabbarzadeh M, Fu HC, Shen Z, Fox JG, Haesebrouck F, et al. Bipolar lophotrichous Helicobacter suis combine extended and wrapped flagella bundles to exhibit multiple modes of motility. Sci Rep 2018;8(1):14415.

[19] Man Y, Page W, Poole RJ, Lauga E. Bundling of elastic filaments induced by hydrodynamic interactions. Phys Rev Fluids 2017;2(12):123101.

[20] Lee W, Kim Y, Griffith BE, Lim S. Bacterial flagellar bundling and unbundling via polymorphic transformations. Phys Rev E 2018;98(5):052405.

[21] Kim M, Bird JC, Parys AJV, Breuer KS, Powers TR. A macroscopic scale model of bacterial flagellar bundling. Proc Natl Acad Sci 2003;100(26):15481–5.

[22] Turner L, Ryu WS, Berg HC. Real-time imaging of fluorescent flagellar filaments. J Bacteriol 2000;182(10):2793–801.

[23] Kudo S, Imai N, Nishitoba M, Sugiyama S, Magariyama Y. Asymmetric swimming pattern of Vibrio alginolyticus cells with single polar flagella. FEMS Microbiol Lett 2005;242(2):221–5.

[24] Fujii M, Shibata S, Aizawa SI. Polar, peritrichous, and lateral flagella belong to three distinguishable flagellar families. J Mol Biol 2008;379(2):273–83.

[25] Cortez R. The method of regularized stokeslets. SIAM J Sci Comput 2001;23(4):1204–25.

[26] Kim M, Powers TR. Deformation of a helical filament by flow and electric or magnetic fields. Phys Rev E 2005;71(2):021914.

[27] Ramia M, Tullock D, Phan-Thien N. The role of hydrodynamic interaction in the locomotion of microorganisms. Biophys J 1993;65(2):755–78.

[28] Berke AP, Turner L, Berg HC, Lauga E. Hydrodynamic attraction of swimming microorganisms by surfaces. Phys Rev Lett 2008;101(3):038102.

[29] Spagnolie SE, Lauga E. Hydrodynamics of self-propulsion near a boundary: predictions and accuracy of far-field approximations. J Fluid Mech 2012;700:105–47.

[30] Lopez D, Lauga E. Dynamics of swimming bacteria at complex interfaces. Phys Fluids 2014;26(7):400–12.

[31] Kirchhoff G. Uber das gleichgewicht und die bewegung eines unendlich dunnen elastischen stabes. J reine angew Math 1859;56:285–313.

[32] Gray J, Hancock G. The propulsion of sea-urchin spermatozoa. J Exp Biol 1955;32(4):802–14.

[33] Lighthill J. Flagellar hydrodynamics. SIAM Rev 1976;18(2):161–230.

[34] Rodenborn B, Chen CH, Swinney HL, Liu B, Zhang H. Propulsion of microorganisms by a helical flagellum. Proc Natl Acad Sci 2013;110(5):E338–47.

[35] Hancock G. The self-propulsion of microscopic organisms through liquids. Proc R Soc London Ser A 1953;217(1128):96–121.

[36] Higdon JJ. The hydrodynamics of flagellar propulsion: helical waves. J Fluid Mech 1979;94(2):331–51.

[37] Johnson RE. An improved slender-body theory for stokes flow. J Fluid Mech 1980;99(2):411–31.

[38] Jawed MK, Khouri NK, Da F, Grinspun E, Reis PM. Propulsion and instability of a flexible helical rod rotating in a viscous fluid. Phys Rev Lett 2015;115(16):168101.

[39] Bergou M, Wardetzky M, Robinson S, Audoly B, Grinspun E. Discrete elastic rods. ACM Trans Graphics (TOG) 2008;27(3):63.

[40] Bergou M, Audoly B, Vouga E, Wardetzky M, Grinspun E. Discrete viscous threads. In: ACM transactions on graphics (TOG), vol. 29. ACM; 2010. p. 116.

[41] Jawed MK, Novelia A, O'Reilly OM. A primer on the kinematics of discrete elastic rods. Springer; 2018.

[42] Jawed MK, Reis PM. Deformation of a soft helical filament in an axial flow at low Reynolds number. Soft Matter 2016;12(6):1898–905.

[43] Jawed M, Reis PM. Dynamics of a flexible helical filament rotating in a viscous fluid near a rigid boundary. Phys Rev Fluids 2017;2(3):034101.

[44] Forghani M., Huang W., Jawed M.K.. Control of uniflagellar soft robots at low Reynolds number using buckling instability. 2018 arXiv preprint arXiv:1810.03113.

[45] Huang W, Jawed M. Numerical exploration on buckling instability for directional control in flagellar propulsion. Soft Matter 2020.

[46] Yamamoto S, Matsuoka T. Dynamic simulation of fiber suspensions in shear flow. J Chem Phys 1995;102(5):2254–60.

[47] Moreau C, Giraldi L, Gadêlha H. The asymptotic coarse-graining formulation of slender-rods, bio-filaments and flagella. J R Soc Interface 2018;15(144):20180235.

[48] Cortez R, Fauci L, Medovikov A. The method of regularized Stokeslets in three dimensions: analysis, validation, and application to helical swimming. Phys Fluids 2005;17(3):031504.

[49] Smith D, Gaffney E, Blake J. Discrete cilia modelling with singularity distributions: application to the embryonic node and the airway surface liquid. Bull Math Biol 2007;69(5):1477–510.

[50] Olson SD, Lim S, Cortez R. Modeling the dynamics of an elastic rod with intrinsic curvature and twist using a regularized stokes formulation. J Comput Phys 2013;238:169–87.

[51] Cortez R. Regularized Stokeslet segments. J Comput Phys 2018;375:783–96.

[52] Peskin CS. The immersed boundary method. Acta Numer 2002;11:479–517.

[53] Fauci LJ, Peskin CS. A computational model of aquatic animal locomotion. J Comput Phys 1988;77(1):85–108.

[54] Stockie JM, Green SI. Simulating the motion of flexible pulp fibres using the immersed boundary method. J Comput Phys 1998;147(1):147–65.

[55] Lim S, Ferent A, Wang XS, Peskin CS. Dynamics of a closed rod with twist and bend in fluid. SIAM J Sci Comput 2008;31(1):273–302.

[56] Lim S. Dynamics of an open elastic rod with intrinsic curvature and twist in a viscous fluid. Phys Fluids 2010;22(2):024104.

[57] Wiens JK, Stockie JM. Simulating flexible fiber suspensions using a scalable immersed boundary algorithm. Comput Methods Appl Mech Eng 2015;290:1–18.

[58] Macnab RM. Bacterial flagella rotating in bundles: a study in helical geometry. Proc Natl Acad Sci 1977;74(1):221–5.

[59] Renda F, Giorgio-Serchi F, Boyer F, Laschi C, Dias J, Seneviratne L. A multi-soft-body dynamic model for underwater soft robots. In: Robotics research. Springer; 2018. p. 143–60.

[60] Kanehl P, Ishikawa T. Fluid mechanics of swimming bacteria with multiple flagella. Phys Rev E 2014;89(4):042704.

[61] Spillmann J, Teschner M. An adaptive contact model for the robust simulation of knots. In: Computer graphics forum, vol. 27. Wiley Online Library; 2008. p. 497–506.

[62] Choe B, Choi MG, Ko HS. Simulating complex hair with robust collision handling. In: Proceedings of the 2005 ACM SIGGRAPH/Eurographics symposium on computer animation. ACM; 2005. p. 153–60.

[63] Gissler M, Becker M, Teschner M. Local constraint methods for deformable objects. In: VRIPHYS; 2006. p. 25–32.

[64] Spillmann J., Becker M., Teschner M.. Non-iterative computation of contact forces for deformable objects. 2007.

[65] Blake J, Chwang A. Fundamental singularities of viscous flow. J Eng Math 1974;8(1):23–9.

[66] Ericson C. Real-time collision detection. CRC Press; 2004.

[67] Kaufman DM, Tamstorf R, Smith B, Aubry J-M, Grinspun E. Adaptive nonlinearity for collisions in complex rod assemblies. ACM Trans Graphics (TOG) 2014;33(4):1–12.

[68] Cai P, Indhumathi C, Cai Y, Zheng J, Gong Y, Lim TS, Wong P. Collision detection using axis aligned bounding boxes. In: Simulations, serious games and their applications. Springer; 2014. p. 1–14.

[69] Redon S, Kheddar A, Coquillart S. Gauss' least constraints principle and rigid body simulations. In: Proceedings 2002 IEEE international conference on robotics and automation (Cat. No. 02CH37292), vol. 1. IEEE; 2002. p. 517–22.

[70] Brochu T, Edwards E, Bridson R. Efficient geometrically exact continuous collision detection. ACM Trans Graphics (TOG) 2012;31(4):1–7.

[71] Masoud H, Stone HA. The reciprocal theorem in fluid dynamics and transport phenomena. J Fluid Mech 2019;879.

[72] Silverman M, Simon MI. Bacterial flagella. Annu Rev Microbiol 1977;31(1):397–419.